Sensors and Materials, Vol. 36, No. 9 (2024) 3645–3661
MYU Tokyo

S & M 3756

Shape Self-sensing Pneumatic Soft Actuator Based on the Liquid-metal Piecewise Curvature Sensor

Zhifang Zhu,[1,2] Ran Zhao,[3] Bingliang Ye,[1*] Pengfei Su,[2] and Longlong Tu[2]

[1]Faculty of Mechanical Engineering, Zhejiang Sci-Tech University, Hangzhou 310000, China
[2]School of Mechanical Engineering, Nanchang Institute of Technology, Nanchang 330099, China
[3]Zhongyuan-Petersburg Aviation College, Zhongyuan University of Technology, Zhengzhou 450000, China

(Received May 7, 2024; accepted July 16, 2024)

Keywords: pneumatic soft actuator, self-sensing, shape estimation, liquid-metal, piecewise strain sensor, K-nearest neighbors algorithm

The shape estimation technique can help solve the end positioning or grasping control of soft robots. However, there is a lack of sensing and modeling techniques for accurate deformation estimation and soft robots with axial elongation, e.g., pneumatic soft actuators (PSAs). This paper presents a shape-self-sensing pneumatic soft actuator (SPSA) with integrated liquid-metal piecewise curvature sensors (LMCSs). Two types of LM composite (Ga–In–Sn/Ga_2O_3 composites for the sensor and Ga–In–Sn/NdFeB/Ni for the electronic wire) were used to build the strain sensor network. Furthermore, a piecewise variable curvature (PVC) model was developed to predict the bending deformation of the soft actuator. A two-SPSAs-based gripper was built to test the identification performance of LMCSs. The results indicate that SPSA could perform contact and size identification using the PVC model. In addition, the K-nearest neighbors (KNN) algorithm was used to classify the shape of the targets. Finally, the circular, triangular, and square targets were identified with an accuracy rate of 93.3%. The work was expected to be applied to the size and shape perception and deformation planning of soft robots.

1. Introduction

Recently, pneumatic soft actuators (PSAs) have been widely used in nondestructive sorting, environment exploration, medical rehabilitation, human–computer interaction, and other fields.[1–4] Their flexibility and stretchability ensure their safety when working towards soft targets. However, high flexibility brings infinite degrees of freedom, which makes it extremely difficult for PSAs to perceive and control their shapes. By far, the deformation control of PSAs usually adopts two traditional methods: open loop control based on the mapping relationship between air pressure and morphology as well as the feedback control based on visual servo.[5,6] The former will fail when the robot interacts with the target (or obstacle) because the pressure corresponds to the expansion of PSAs. The latter relies on visual sensors and image analysis

*Corresponding author: e-mail: zist_ybl@zstu.edu.cn
https://doi.org/10.18494/SAM5094

ISSN 0914-4935
https://myukk.org/

algorithms, which are easily affected by natural conditions such as lighting and occlusion. Adopting a non-visual shape perception strategy is a better choice for continuous soft robots.

PSAs can achieve the ontology perception of bending deformation by integrating strain sensors. Metal film resistance gauges were the first strain sensors considered. For example, Shu *et al*. embedded strain gauges into a pneumatic soft gripper for the target's size identification.[7] However, introducing non-stretchable structures will cause the failure of PSAs owing to the generation of interface cracks. After that, flexible and stretchable materials are most widely considered. For example, carbon nanotubes and liquid-metal composites have been reported to be used as integrable strain sensors for bending measurements by coating or depositing them on the actuator's surface.[8,9] In addition to this, magnetic or fluid-based strain sensors have also been developed for deformation sensing.[10,11] However, these sensors typically feature more complex structures, which can increase the manufacturing complexity of self-sensing piezoelectric actuators. PSAs can achieve a perceptual estimation of their shape by configuring a single flexible strain sensor and using simple models such as constant curvature equations.[12]

However, PSAs face difficulties in complex tasks, e.g., the end effector control of flexible robotic arms, the propulsion of continuum robots in complex environments, and the gripping interactions of soft grippers. A piecewise constant curvature model can help PSAs achieve a more precise shape perception, but more strain sensors are required.[13,14]

In summary, designing a strain sensor network for precise shape perception is still a significant challenge. Researchers need to consider the interface mismatch between sensors and PSAs, as well as the modeling problem of shape estimation. The work presented a piecewise strain sensor network based on liquid-metal composites. A piecewise variable curvature model has been developed for shape perception under complex deformations. We validated the performance of the sensor and model using a two-finger pneumatic soft gripper. The details are provided in the following sections.

2. Methodology

2.1 Principle

Figure 1 shows the working principle of the self-sensing PSA. An all-in-one liquid-metal piecewise sensor is integrated with the PSA [Figure 1(a)]. The liquid-metal piecewise curvature sensor (LMCS) is located on the upper surface of the PSA's constraint layer to obtain greater tension during actuator bending deformation. For the constraint layer, the same material as that for the PSA is used to achieve reliable adhesion. Figure 1(b) shows the details of the three-resistor serial network, and two different LM composites are used for sensors and flexible wires. The proposed self-sensing PSA is designed for target contact, size, and shape identification. Figure 1(c) presents the working principle of a two-PSA-based gripper. When the gripper interacts with the target object, LMPS perceives the curvature changes in different areas of the PSA. The implementation of curvature perception is based on the proposed PVC model. Furthermore, the hyperelastic, microchannel, and PSA dynamic models are used to construct a complete perception model. Different identification strategies (including those based on basic

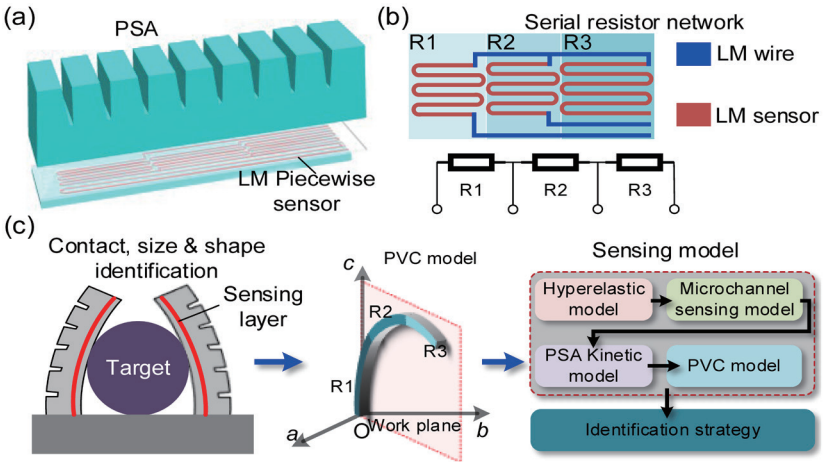

Fig. 1. (Color online) Liquid-metal piecewise strain sensor for PSA deformation self-sensing: (a) PSA integrated with LMCS, (b) serial sensor network, and (c) curvature sensing model for target identification.

perception models and those assisted by classification algorithms) are used to achieve the perception of the target contact, size, and shape.

2.2 Materials and fabrication

Figure 2 shows the fabrication method for the proposed LMCS using two types of LM composite, i.e., Ga–In–Sn/Ga_2O_3 and Ga–In–Sn/Ni/NdFeB composites, used as raw materials for sensors and wires, respectively. As reported in Refs. 15 and 16, metal oxides and particles can be used to regulate the mechanical, electrical, and magnetic properties of liquid metals. By modifying them, the surface tension of the liquid metal is greatly reduced, while it exhibits good adhesion and wetting properties. Filling liquid metal composite materials into microchannels can prevent the leakage of the liquid metal and improve the reliability of sensors and liquid metal circuits.

The Ga–In–Sn/Ga_2O_3 composite is used as the sensing material for LMCS. Ga_2O_3 particles can reduce the electrical resistivity of Ga-based alloys, and Ga_2O_3 is also generated during mechanical stirring, which rapidly achieves the encapsulation of Ga_2O_3 particles by the liquid metal and the formation of a stable composite porous structure [Fig. 2(a)]. Our previous work proposed a patternable, stretchable liquid metal electronic wire made of the Ga–In–Sn/Ni/NdFeB composite.[16] This material is not sensitive to pressure or tension, which makes it an ideal material for flexible electronic wires in sensors.

Figure 2(b) shows that Ga–In–Sn/Ga_2O_3 composites are prepared by grinding. Ga–In–Sn and Ga_2O_3 at a mass ratio of 6:4 are ground using corundum mortar and pestle in air for 10 min. Ga–In–Sn/Ni/NdFeB composites are prepared by mechanical stirring.[16] Ga–In–Sn, Ni, and NdFeB are placed in a container at a mass ratio of 5:2:3 and stirred for 30 min with a mechanical stirrer. The conductivities of the Ga–In–Sn/Ga_2O_3 and Ga–In–Sn/Ni/NdFeB composites are 0.86×10^6 and 1.44×10^6 S/m, respectively.

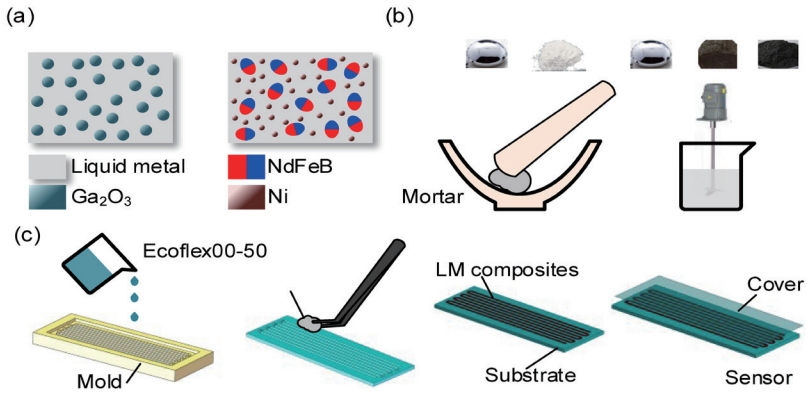

Fig. 2. (Color online) Fabrication of liquid-metal piecewise strain sensor: (a) microstructures of LM/Ga_2O_3 and LM/NdFeB/Ni, (b) preparation process for the two composites, and (c) preparation process for LMCS.

Table 1 shows the parameters of the materials used for LMCS. $Ga_{68.5}In_{21.5}Sn_{10}$ with a melting point of −19 °C was utilized to fabricate the two composites. The extremely low phase-transition temperature allows the sensor to be used in environments below 0 °C, which is superior to most reported liquid metal sensors. Ga_2O_3 has a lower conductivity than elemental gallium and can improve the sensing performance of the LM/Ga_2O_3 composites. By using NdFeB, we constructed a stable porous structure and utilized Ni particles to improve the material's conductivity and magnetism. This composite material has a stronger locking capability for liquid metals than traditional LM/NdFeB composites.

A serial liquid-metal sensor network is developed by filling the liquid metal into microchannels. Figure 2(c) shows that the prepared LM composites are filled into the microchannels of the silicone substrate and then sealed with a silicone cover. The depth and width of the microchannels were 300 and 400 μm, respectively. The length of each LMCS was 30 mm.

3. Model

3.1 Hyperelastic model

The Mooney–Rivlin model is used to describe the deformation of the proposed PSA. The strain energy density function $\boldsymbol{W}$ can be expressed as[17]

$$\boldsymbol{W} = W(I_1, I_2, I_3), \tag{1}$$

$$\begin{cases} I_1 = \lambda_1^2 + \lambda_2^2 + \lambda_3^3 \\ I_2 = \lambda_1^2\lambda_2^2 + \lambda_2^2\lambda_3^3 + \lambda_3^3\lambda_1^2 \\ I_3 = \lambda_1^2\lambda_2^2\lambda_3^2 \end{cases}, \tag{2}$$

$$\lambda_i = 1 + \varepsilon_i, \tag{3}$$

Table 1
Material parameters of LMCS.

Materials	Parameters			
$Ga_{68.5}In_{21.5}Sn_{10}$	Melting point (°C)	Conductivity (S/m)	Density (g/cm^3)	Surface tension (N/m)
	−19	3.46×10^6	6.3	0.7
Ga_2O_3	Particle size (μm)	Conductivity (S/m)	Density (g/cm^3)	
	5–7	1.1	6.4	
NdFeB	Particle size (μm)	Conductivity (S/m)	Density (g/cm^3)	Magnetic energy product (MOe)
	6	0.6×10^5	7.6	16.2
Ni	Particle size (μm)	Conductivity (S/m)	Density (g/cm^3)	Permeability
	500	2.4×10^5	7.1	202

where I_1, I_2, and I_3 are the first, second, and third invariants of the deformation tensor, respectively; λ_i is the main elongation ratio of the material; and ε_i is the main axis strain.

Assuming that the deformation of the silicone material is isotropic and uniform, the strain energy density function can be expressed as an N-order polynomial as follows:

$$W = \sum_{i,j=1}^{N} C_{ij}(I_1 - 3)^i (I_2 - 3)^j + \sum_{i=1}^{N} \frac{1}{D_i}(J-2)^{2i}\ , \tag{4}$$

where C_{ij} is the Rivlin coefficient; D_i is the incompressibility parameter; J is the volume change ratio ($J = \lambda_1\lambda_2\lambda_3$).

The elastic strain energy of the two-parameter Mooney–Rivlin model can be expressed as

$$W = C_{10}(I_1 - 3) + C_{01}(I_2 - 3)\,. \tag{5}$$

According to Eq. (5), the Cauchy stress in the uniaxial direction is defined by

$$\sigma_1 = 2(\lambda_1 - \frac{1}{\lambda_1^2})C_{10} + 2(1 - \frac{1}{\lambda_1^3})C_{01}\,. \tag{6}$$

On the basis of the assumption of incompressibility of materials, the volume change rate J is 1. The following constraints can be obtained:

$$\lambda_2 = \lambda_3 = \frac{1}{\sqrt{\lambda_1}}\,. \tag{7}$$

3.2 Microchannel strain sensing model

Since LM magnetic mud is a plastic material, its shape is consistent with the shape of the microchannel. Therefore, the resistance model of LM composites can be obtained by analyzing

the deformation of microchannels. We assume that silicone and LM composites are both incompressible materials, and the lateral deformation of the microchannel is uniform when the strain of the sensor does not exceed 20%. The total volume V of the microchannel remains unchanged before and after stretching. According to Fig. 3(a),[18]

$$V = l_0 h_0 w_0 = lhw, \tag{8}$$

where l_0, h_0, and w_0 are the length, thickness, and width of the microchannel before stretching; l, h, and w are those after stretching, respectively.

According to the definition of electrical resistivity,

$$R = \rho \frac{l}{wh}, \tag{9}$$

where ρ is the electrical resistivity of LM composites.

As illustrated in Figure 3(b), when considering a serpentine shape, the resistor can be divided into two parts: one that runs parallel to the stretching direction and the other that is perpendicular to it. The resistances of these two parts are $R_{//}$ and $R_{\perp}$, respectively. The global resistance can be defined by

$$R = \gamma R_{//} + (1-\gamma) R_{\perp}, \tag{10}$$

where γ is the proportion of the parallel microchannel (along the stretching direction).

On the basis of the serpentine-shaped structure [Fig. 3(b)], the elongation of the strain sensor leads to an anisotropic deformation of the microchannels. This means that the dimensions of the microchannels behave differently depending on their orientation relative to the direction of elongation. Therefore, the parallel and perpendicular microchannels' dimension variations can be expressed as

$$\begin{cases} l_{//} = \lambda_1 l_0 \\ w_{//} h_{//} = \dfrac{1}{\lambda_1} w_0 h_0 \end{cases}, \tag{11}$$

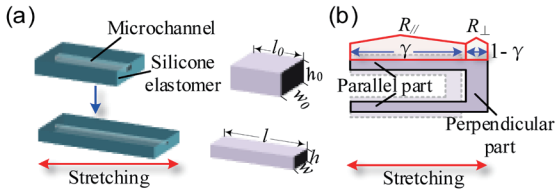

Fig. 3. (Color online) Microchannel strain sensor model: (a) microchannel and (b) resistance model.

$$\begin{cases} l_{\perp} = \dfrac{1}{\sqrt{\lambda_1}} l_0 \\ w_{\perp} h_{\perp} = \sqrt{\lambda_1} w_0 h_0 \end{cases}. \tag{12}$$

Using Eqs. (9), (11), and (12), the expressions for $R_{//}$ and $R_{\perp}$ can be derived as

$$R_{//} = \gamma \lambda_1^2 \rho \frac{l_0}{w_0 h_0}, \tag{13}$$

$$R_{\perp} = (1-\gamma) \frac{1}{\lambda_1} \rho \frac{l_0}{w_0 h_0}. \tag{14}$$

According to Eq. (10), the global resistance R can be written as

$$R = \left[\gamma \lambda_1^2 + (1-\gamma) \frac{1}{\lambda_1} \right] \rho \frac{l_0}{w_0 h_0}. \tag{15}$$

Ignoring the variation of vertical resistance, the sensor strain is given as

$$\lambda_1 = \sqrt{R \frac{w_0 h_0}{\gamma \rho l_0} - \frac{1}{\gamma} + 1}. \tag{16}$$

3.3 Piecewise variable curvature model

We established the piecewise variable curvature model to predict the deformation of the PSA (Fig. 4). A multi-chamber bending deformation sensing unit is given in Fig. 4(a). Here, a sensing unit is composed of three (not limited to this number) air chambers, a constraint layer, and a sensing layer (includes a single LM sensor). L_0, l_i, and L_i are the bottom arc length of the constraint layer, sensing layer, and axial centerline, respectively. H_0 is the thickness of the constraint layer and H_1 is the thickness of the sensing layer from the centerline. r_0 and r_i are the radii corresponding to arcs L_0 and L_i, respectively, and θ_i is the bending angle.

When applying the pressure p, it is assumed that the arc length l_0 at the bottom of the constraint layer remains unchanged. We can obtain the following geometric relationship:

$$\begin{cases} r_i = H_1 + H_0 + r_0 \\ l_0 = \theta_i \cdot r_0 \\ l_i = \theta_i \cdot (H_0 + r_0) \\ L_i = \theta_i \cdot (H_1 + H_0 + r_0) \end{cases}. \tag{17}$$

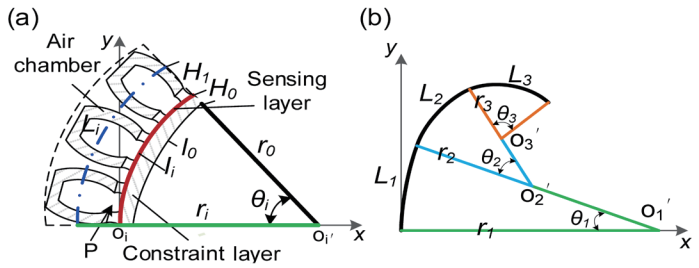

Fig. 4. (Color online) Piecewise variable curvature model: (a) multi-chamber deformation sensing unit and (b) piecewise variable curvature model.

Here, we use the centerline L_i equivalent to the PSA and assume the main elongation ratios of the PSA as λ_1', λ_2', and λ_3'. According to Eq. (17), the axial elongation of the PSA can be expressed as

$$\lambda_1' = \frac{L_i}{l_0} = \frac{l_0 + \theta_i(H_1 + H_0)}{l_0}, \tag{18}$$

$$\lambda_1' = \lambda_1\left(1 + \frac{\theta_i H_1}{l_0 + \theta_i H_0}\right). \tag{19}$$

After the bending deformation of the soft drive, the axial and initial cross-sectional areas can be obtained by calculating[19]

$$s = s_0 \lambda_2' \lambda_3', \tag{20}$$

where s and s_0 are the axial and initial cross-sectional areas, respectively.

The force balance equation is formulated according to the shape of the soft drive section, and the relationship between the main stress and the driving pressure is deduced as

$$\sigma_1 = \frac{p}{\lambda_2' \lambda_3'}. \tag{21}$$

Equations (17), (18) and (20) are substituted into Eq. (6) to obtain the relationship between the bending angle and the driving pressure as

$$\theta_i = \frac{l_0}{(H_1 + H_0)}\left(\sqrt[3]{\frac{2C_{10}}{2C_{10} - p}} - 1\right). \tag{22}$$

According to Eq. (22), Eq. (18) can be defined by

$$\lambda_1{}' = 1 + \left(\sqrt[3]{\frac{2C_{10}}{2C_{10} - p}} - 1 \right). \tag{23}$$

According to the curvature formula, we have

$$r_i = \frac{L_i}{\theta_i} = (H_1 + H_0)\left(\frac{1}{\left(\sqrt[3]{\frac{2C_{10}}{2C_{10} - p}} - 1 \right)} + 1\right). \tag{24}$$

Now we have the model of a multi-chamber bending-sensing unit, and Eq. (24) indicates that its bending radius is related to the driving pressure in the natural state (noncontact). According to the model given in Fig. 4(a), Eq. (16) is used to derive the curvature equation with the strain resistance R as the independent variable as follows.

$$\theta_i = \frac{l_0}{H_0}\left(\sqrt{R\frac{w_0 h_0}{\gamma \rho l_0} - \frac{1}{\gamma} + 1} - 1 \right) \tag{25}$$

$$L_i = l_0\left(\frac{H_1 + H_0}{H_0} \sqrt{R\frac{w_0 h_0}{\gamma \rho l_0} - \frac{1}{\gamma} + 1} - \frac{H_1}{H_0} \right) \tag{26}$$

As shown in Fig. 4(b), L_1, L_2, and L_3 are the lengths of the three arcs; r_1, r_2, and r_3 and θ_1, θ_2, and θ_3 are the radii and bending angles of the three arcs, respectively. Therefore, the parameter equation for the deformation curve of the PSA can be expressed as

$$x = \begin{cases} a_1 - r_1 \cos\alpha & 0 \le \alpha < \theta_1 \\ a_2 - r_2 \cos\alpha & \theta_1 \le \alpha \le \theta_1 + \theta_2 \\ a_3 - r_3 \cos\alpha & \theta_1 + \theta_2 < \alpha \le \theta_1 + \theta_2 + \theta_3 \end{cases}, \tag{27}$$

$$y = \begin{cases} b_1 + r_1 \sin\alpha & 0 \le \alpha < \theta_1 \\ b_2 + r_2 \sin\alpha & \theta_1 \le \alpha \le \theta_1 + \theta_2 \\ b_3 + r_3 \sin\alpha & \theta_1 + \theta_2 < \alpha \le \theta_1 + \theta_2 + \theta_3 \end{cases}, \tag{28}$$

where

$$\begin{aligned} &a_1 = 0,\ b_1 = r_1, \\ &a_2 = r_1 - (r_1 - r_2)\cos\theta_1,\ b_2 = (r_1 - r_2)\sin\theta_1, \\ &a_3 = r_1 - (r_1 - r_2)\cos\theta_1 - (r_2 - r_3)\cos(\theta_1 + \theta_2), \\ &b_3 = (r_1 - r_2)\sin\theta_1 + (r_2 - r_3)\sin(\theta_1 + \theta_2). \end{aligned} \tag{29}$$

3.4 Contact, size and shape identification

3.4.1 Contact identification

In Sect. 3.3, two sets of curvature estimation equations are obtained for describing PSA bending. The two sets of equations take the pressure p and the strain resistance R as inputs. In this section, we will discuss how to use these two sets of equations for size estimation. Equations (22)–(24) will fail when contact behavior occurs. When PSA interacts with other objects, its curvature is smaller than that of the free deformation. Equations (25) and (26) can provide more accurate solutions to curvature equations because strain sensors are used to directly measure the variation of PSA's arc length. Therefore, whether or not contact occurs does not affect its perception of curvature. However, this does not mean that the first set of equations has lost PSA's usefulness. Figure 5 presents a differential sensing strategy for contact sensing based on those two sets of equations.

Figure 5(a) shows the deformations of PSA under contact and noncontact conditions. Figure 5(b) presents the variation curves of pressure and sensor resistors during the bending process upon contact, and the strain resistance will no longer change. Figure 5(c) provides the details of using the differential sensing strategy for contact sensing. Two sets of curvature equations are used to calculate the curvature of PSA, and a threshold switching function is used to make a judgment. When the threshold is exceeded, contact has occurred. The contact function is given as

$$Contact = \begin{cases} 1 & \text{when } \Delta\kappa > Treshold_C \\ 0 & \text{when } \Delta\kappa \le Treshold_C \end{cases}, \tag{30}$$

and

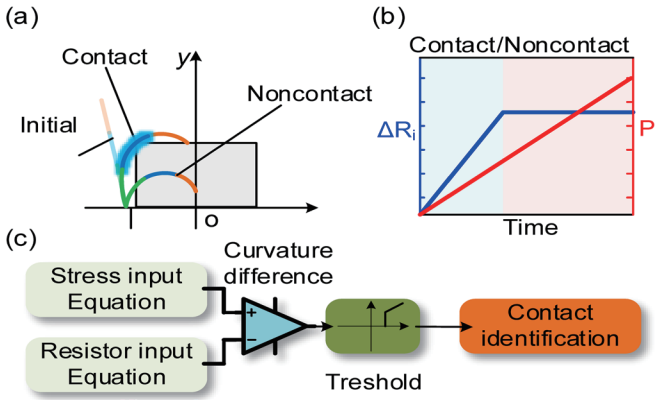

Fig. 5. (Color online) Size identification method: (a) contact and noncontact deformations, (b) two-finger structure gripper for size identification, and (c) differential sensing strategy.

$$\Delta\kappa = \kappa_r - \kappa_p \,. \tag{31}$$

where κ_p and κ_r are the curvatures calculated on the basis of resistance and pressure, respectively, and $\kappa = 1/r$. The threshold function takes 5% of the maximum curvature.

3.4.2 Size estimation

In this section, we propose a size identification strategy based on the two-finger gripper structure. As shown in Fig. 6, assuming that the inclination angle of PSA is β and the length of the PSA is L, (x_a, y_a) and (x_b, y_b) are the end coordinates of the two-finger gripper; the bottom opening distance of the gripper is q and the top opening distance is Q. Then, $Q = 2(L\cos(\pi - \theta))$.

The estimated diameter of the target can be defined by

$$d = \left| x_b - x_a \right|_{max} . \tag{32}$$

3.4.3 Shape identification

A shape identification method is developed on the basis of the LMCS (Fig. 7). Utilizing the curvature data derived from the LMCS, we can determine the shape of the piezoelectric self-sensing actuator. This information can then be employed to distinguish between triangular, square, and circular targets. Here, the K-nearest neighbors (KNN) algorithm is used to classify the target shape. Figure 7 shows that the segmented sensor resistors of two LMCSs are defined as R_{a1}, R_{a2}, R_{a3}, R_{b1}, R_{b2}, and R_{b3}. These six resistance values are used as features for the KNN algorithm for classifying.

4. Results and Discussion

4.1 Numerical analysis

According to the mathematical model given in Sect. 3, we perform a numerical analysis of the LM sensor and self-sensing PSA. For simulation, the following parameters are given. The

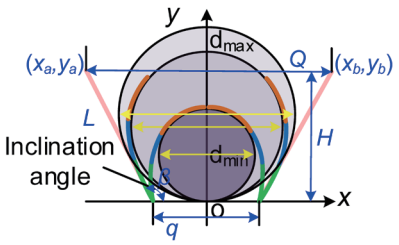

Fig. 6. (Color online) Size identification method.

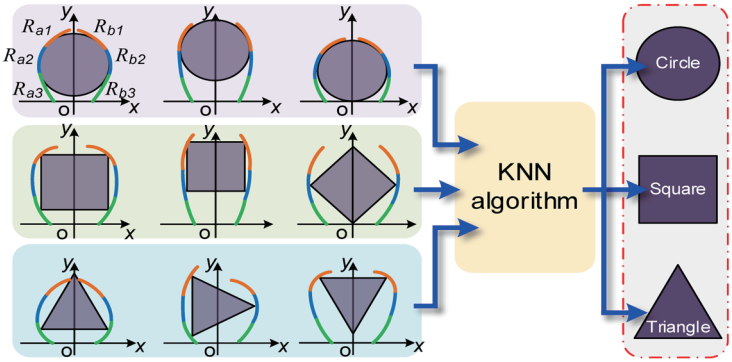

Fig. 7. (Color online) Shape identification method.

total length L of the PSA is 100 mm. The thicknesses of H_0 and H_1 are 4 and 11 mm, respectively. The resistivity ρ is 0.0000073 Ω/m and C_{10} = 0.12 MPa. Figure 8 shows the calculation results.

4.2 Material characterization

The particles and composites used for preparing the LMCS in this work are observed by scanning electron microscopy (SEM). Figure 9(a) shows the SEM images of Ga_2O_3 particles and the Ga_2O_3/Ga–In–Sn composite. Figure 9(b) exhibits the SEM images of Ni particles, NdFeB particles, and the NdFeB/Ga–In–Sn composite. Here, the diameter of Ni microspheres was made smaller than that of NdFeB particles to ensure that Ni particles can be adsorbed around NdFeB particles.

4.3 Sensor performance

The LMCS was tested to investigate its performance. Figure 10(a) shows the fabricated sensor and the PSA with the LMCS. Figure 10(b) shows the tensile change curve of the LMCS. It was found that the change in R_3 is slightly smaller than those in R_1 and R_2. This is because R_3 is at the end of the resistor, and its wire is longer. Figure 10(c) provides test results for the self-sensing PSA. When the air pressure changes at 0–30 kPa, the range of LMCS resistance variations is 0–90 mΩ.

4.4 Contact, size and shape identification results

Figure 11 shows the actual and simulation results of deformation when different areas of PSA come into contact with the target object. According to the distribution of the LMCS on the PSA, the PSA is divided into three regions: bottom, middle, and top. Here, the threshold is 0.5. The identification results are given in Table 2.

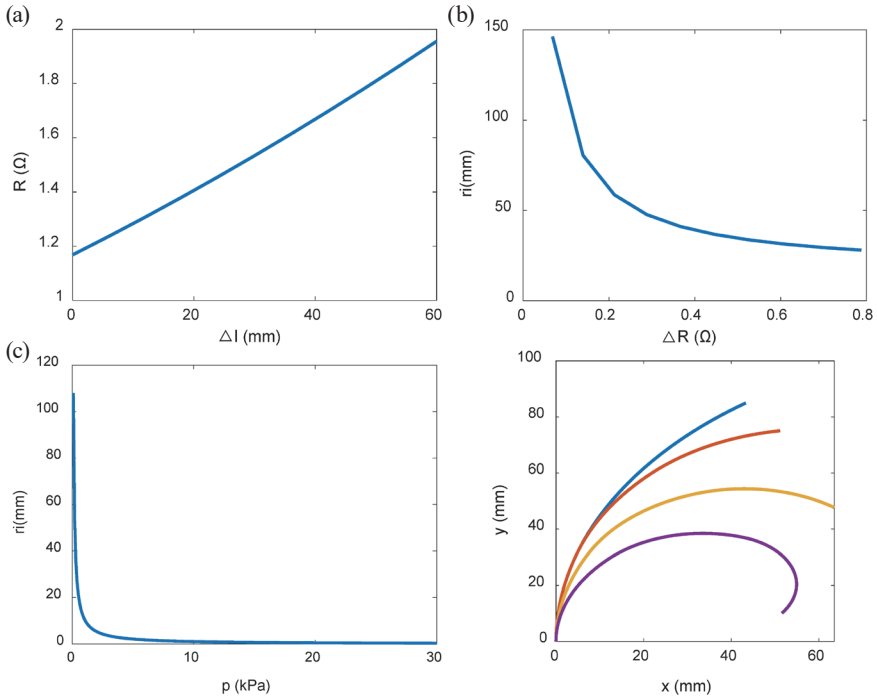

Fig. 8. (Color online) Numerical calculation results: (a) R versus axial tension, (b) curves of curvature radius r_i and R, (c) r_i versus pressure p, and (d) bending shape.

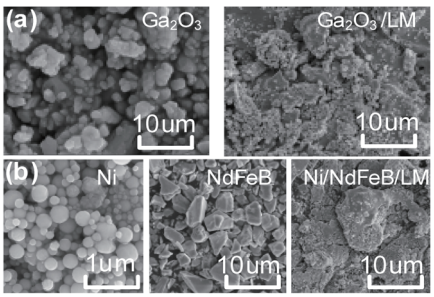

Fig. 9. SEM images of (a) Ga_2O_3 particles and Ga_2O_3/Ga–In–Sn composite and (b) Ni particles, NdFeB particles and Ni/NdFeB/Ga–In–Sn composite.

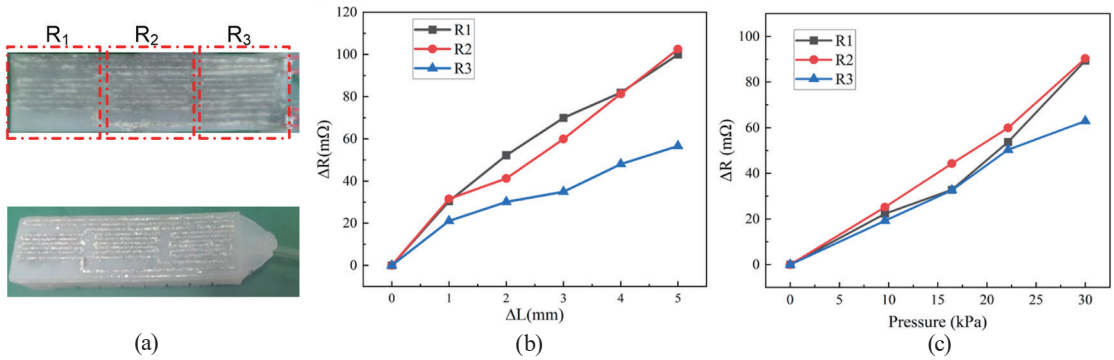

Fig. 10. (Color online) Sensor performance: (a) prepared LMCSs, (b) tensile change curves of LMCSs, and (c) air pressure change curves of LMCSs.

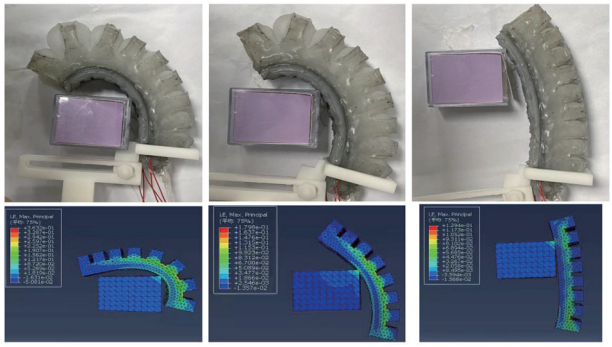

Fig. 11. (Color online) Contact identification

Table 2
Curvature differential identification results.

Contact area	Differential value			Results
	$\kappa p_1 - \kappa r_1$	$\kappa p_2 - \kappa r_2$	$\kappa p_3 - \kappa r_3$	
Bottom	$\kappa p_1 - \kappa r_1 < Treshold_C$	$\kappa p_2 - \kappa r_2 > Treshold_C$	$\kappa p_3 - \kappa r_3 > Treshold_C$	1
Middle	$\kappa p_1 - \kappa r_1 > Treshold_C$	$\kappa p_2 - \kappa r_2 < Treshold_C$	$\kappa p_3 - \kappa r_3 > Treshold_C$	1
Top	$\kappa p_1 - \kappa r_1 > Treshold_C$	$\kappa p_2 - \kappa r_2 > Treshold_C$	$\kappa p_3 - \kappa r_3 < Treshold_C$	1

Table 2 shows the curvature differential identification results of different areas. According to Eq. (31), the curvature difference of each segment was calculated separately and compared with threshold. The area of contact was determined on the basis of comparison results.

Figure 12 shows the experimental results of target size identification. We chose three cups of different sizes (32, 54 and 62 mm) as the gripping targets. The identification results are given in Table 3. The estimation error is less than 5%. The predicted results for the largest ball are slightly higher than the actual values, which is different from the two predicted results. As the object's size approaches the gripper's opening distance, which defines the upper limit of what the gripper can accurately estimate, the precision of the prediction outcomes is likely to diminish.

Figure 13 shows the experimental results of target shape identification. An industrial multichannel resistance acquisition module (a resolution of 0.1 mΩ and a sampling frequency of 100ms) was used to collect the resistance of the LMCS. Resistance data during the grasping process are saved for offline training. Figure 13(a) shows the deformation results of the soft gripper in grasping targets of different shapes. The real-time resistance variations of six LM sensors are shown in Fig. 13(b). Figure 13(c) shows the confusion matrix obtained from the Matlab classification learner. The prediction accuracy reached 93.3%.

5. Conclusion

The work presented LMCSs for the shape self-sensing of PSAs. The LMCSs were manufactured using microchannel technology. Two modified LM-compliant materials were used to replace pure liquid metals. A PVC model was also developed to help estimate the bending shape. Finally, comprehensive simulations and experiments have confirmed that self-sensing

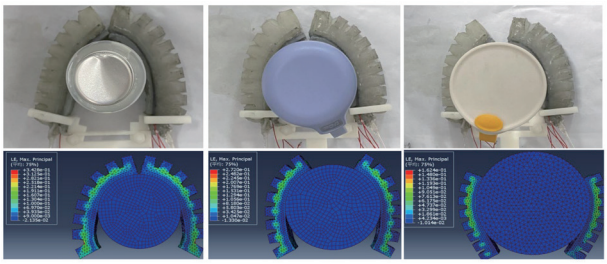

Fig. 12. (Color online) Size identification results of cups A, B, and C.

Table 3
Size identification results.

Target	Actual diameter (mm)	Identification diameter (mm)
Cup A	32	29.4
Cup B	54	51.1
Cup C	62	63.5

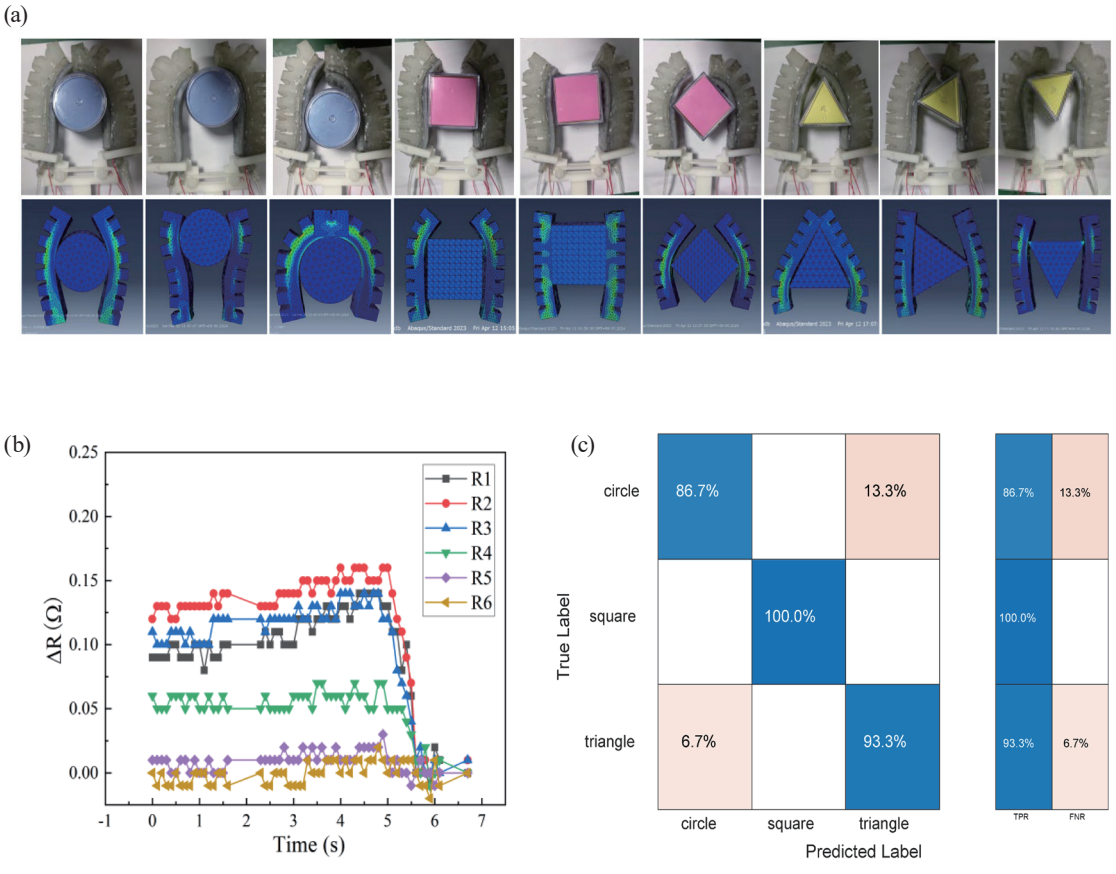

Fig. 13. (Color online) Shape identification results: (a) deformation when grabbing different targets, (b) real-time data of six resistors, and (c) KNN classification results.

actuators were capable of detecting contact, size, and shape. The main contributions of this work are as follows.

(1) Design of piecewise curvature sensors based on two types of liquid metal composite (Ga–In–Sn/Ga_2O_3 and Ga–In–Sn/NdFeB/Ni).
(2) Proposal of a piecewise constant curvature model based on LMCS.
(3) Design of a PSA integrating LMCS and proposal of a target identification method based on LMCS.
(4) Our future work will explore the integration of tactile and shape perceptions to enhance PSA's ability to perform tasks.

Acknowledgments

This work was supported by the Special Fund for Basic Scientific Research Business of Zhongyuan University of Technology (Grant No. K2022YY008) and the Major Science and Technology Research and Development Project of Jiangxi Province (Grant No. 20233AAE02003).

References

1 A. Rajappan, B. Jumet, and D. J. Preston: Sci. Rob. **6** (2023) 51. https://doi.org/10.1126/scirobotics.abg6994.
2 Z. Tang, J. Lu, Z. Wang, W. Chen, and H. Feng: Auton. Rob. **44** (2020) 2. https://doi.org/10.1007/s10514-019-09892-x.
3 P. H. Nguyen and W. Zhang.: Sci. Rep. **10** (2020) 1. https://doi.org/10.1038/s41598-020-65003-2.
4 M. Takaiwa: J. Jpn. Fluid Power Syst. Soc. **39** (2008) 320. https://ndlsearch.ndl.go.jp/books/R000000004-I9719356.
5 S. Chen, H. Xu, F. Haseeb, W. Fan, and Q. Wei: Sens. Actuators, A **356** (2023). https://doi.org/10.1016/j.sna.2023.114284.
6 Y. Wang, H. Wang, and W. Chen: Jiqiren/Robot. **40** (2018) 5. https://doi.org/10.13973/j.cnki.robot.180378.
7 S. Shu, Z. Wang, P. Chen, J. Zhong, W. Tang, and Z. L. Wang: Adv. Mater. **35** (2023) 18. https://doi.org/10.1002/adma.202211385.
8 H. Yang, Y. Chen, Y. Sun, and L. Hao: Sens. Actuators, A **266** (2017) 318. https://doi.org/10.1016/j.sna.2017.09.040.
9 I. S. Godage, D. T. Branson, E. Guglielmino, G. A. Medrano-Cerda, and D. G. Caldwell: Proc. 2011 IEEE Int. Conf. Robot Autom. (IEEE, 2011) 452–457.
10 Q. Shu, G. Liao, S. Liu, H. Deng, H. Pang, Z. Xu, X. Gong, and S. Xuan: Adv. Mater. Technol. **8** (2023) 2300019. https://doi.org/10.1002/admt.202300019.
11 A. Koivikko, V. Lampinen, M. Pihlajamäki, K. Yiannacou, V. Sharma, and V. Sariola: Commun. Eng. **1** (2022) 1. https://doi.org/10.1038/s44172-022-00015-6.
12 R. J. Webster III and B. A. Jones: Int. J. Rob. Res. **29** (2010) 13. https://doi.org/10.1177/0278364910368147.
13 R. K. Katzschmann, C. Della Santina, Y. Toshimitsu, A. Bicchi, and D. Rus: Proc. 2019 2nd IEEE Int. Conf. Soft Robot (RoboSoft) (IEEE, 2019) 454–461.
14 F. Xu, D. Ning, W. Hongtao, D. Longwei, and X. Shaohui: Chin. J. Mech. Eng. **31** (2020) 9. https://doi.org/10.3969/j.issn.1004-132X.2020.09.013.
15 D. Wang, X. Wang, and W. Rao: Acc. Mater. Res. **2** (2021) 1093. https://doi.org/10.1021/accountsmr.1c00173.
16 Z. Zhu, R. Zhao, B. Ye, and H. Wang: AIP Adv. **13** (2023) 115221. https://doi.org/10.1063/5.0158221.
17 H. Jiang, Z. Wang, X. Liu, X. Chen, Y. Jin, X. You, and X. Chen: Proc. 2017 IEEE Int. Conf. Robot Autom (ICRA) (IEEE, 2017) 6127–6133.
18 F. Pineda, F. Bottausci, B. Icard, L. Malaquin, and Y. Fouillet: Microelectron. Eng. **144** (2015) 27. https://doi.org/10.1016/j.mee.2015.02.013.
19 M. Li, M. Ning, and H. Chen: Chin. J. Mech. Sci. Technol. **40** (2021) 33. https://doi.org/10.13433/j.cnki.1003-8728.20190344.

About the Authors

Zhifang Zhu is now a doctoral student at Zhejiang Sci-Tech University in China. He is also an associate professor at Nanchang Institute of Technology. His main research direction is intelligent perception. (zhuzhifang1984@163.com)

Ran Zhao is currently an associate professor at Zhongyuan University of Technology in China. His main research interest is in soft robots. (zhaoran@zut.edu.cn)

Bingliang Ye is currently a doctoral supervisor and professor at Zhejiang Sci-Tech University in China. His main research interest is in agricultural robots. (zist_ybl@zstu.edu.cn)

Pengfei Su is now a master's student at Nanchang Institute of Technology in China. His main research direction is the structural design of soft robots. (spf3244596455@163.com)

Longlong Tu is now a master's student at Nanchang Institute of Technology in China. His main research directions are the design and control aspects of soft robots.
(tll2019101649@163.com)